

Intrinsic Second-Order Topological Superconductors with Tunable Majorana Zero Modes

Xiao-Jiao Wang,^{1,2,3} Yijie Mo,^{1,2,3} Zhi Wang,^{1,2} Zhigang Wu,^{4,*} and Zhongbo Yan^{1,2,3,†}

¹School of Physics, Sun Yat-sen University, Guangzhou 510275, China

²Guangdong Provincial Key Laboratory of Magnetolectric Physics and Devices, Sun Yat-sen University, Guangzhou 510275, China

³State Key Laboratory of Optoelectronic Materials and Technologies, Sun Yat-sen University, Guangzhou 510275, China

⁴Quantum Science Center of Guangdong-Hong Kong-Macao Greater Bay Area (Guangdong), Shenzhen 508045, China

(Dated: December 3, 2025)

Dirac semimetals, with their protected Dirac points, present an ideal platform for realizing intrinsic topological superconductivity. In this work, we investigate superconductivity in a two-dimensional, square-lattice nonsymmorphic Dirac semimetal. In the normal state near half-filling, the Fermi surface consists of two distinct pockets, each enclosing a Dirac point at a time-reversal invariant momentum ($\mathbf{X} = (\pi, 0)$ and $\mathbf{Y} = (0, \pi)$). Considering an on-site repulsive and nearest-neighbor attractive interaction, we use self-consistent mean-field theory to determine the ground-state pairing symmetry. We find that an even-parity, spin-singlet $d_{x^2-y^2}$ -wave pairing is favored as it gives rise to a fully gapped superconducting state. Since the pairing amplitude has opposite signs on the two Dirac Fermi pockets, the superconducting state is identified as a second-order topological superconductor. The hallmark of this topological phase is the emergence of Majorana zero modes at the system's boundaries. Notably, the positions of these Majorana modes are highly controllable and can be manipulated simply by tailoring the boundary sublattice terminations. Our results highlight the promise of nonsymmorphic Dirac semimetals for realizing and manipulating Majorana modes.

Topological superconductors (TSCs) are highly sought-after materials for hosting Majorana zero modes (MZMs) [1–8]. The non-Abelian statistics of these quasiparticles offer a promising route to fault-tolerant topological quantum computation [9–12]. Over the past two decades, guided by pioneering theoretical work [13–19], significant progress has been made in engineering topological superconducting phases, principally by proximitizing topological insulators [20–22], magnetic chains [23, 24] or semiconducting nanowires [25–28] with conventional s -wave superconductors. However, these heterostructure approaches currently face significant challenges [29–32], including impurity-induced degradation of sample quality, small superconducting gaps, and the presence of trivial bound states whose experimental signatures can resemble those of MZMs. The discovery of intrinsic TSCs—those that do not rely on proximity effects—offers a route to mitigating these issues, as such systems generally promise larger superconducting gaps and lower levels of disorder.

Topological materials that become superconducting below a critical temperature are promising candidates for intrinsic TSCs. A prominent example is provided by certain three-dimensional iron-based superconductors which feature topologically inverted band structures and Dirac surface states [33–37]. In these materials, compelling evidence for MZMs has been observed at vortex line ends [38–41]. Despite this progress, manipulating MZMs in such materials remains a major experimental challenge, underscoring the need for intrinsic TSCs capable of hosting highly tunable Majorana modes.

In the search for intrinsic TSCs, the Fermi surface and pairing symmetry are two key factors to consider [42–44]. While odd-parity spin-triplet pairings or phase-winding pairings (e.g., $d \pm id$) naturally give rise to topological superconductivity [45–50], materials that host such exotic pairing states are exceedingly rare and typically have very low

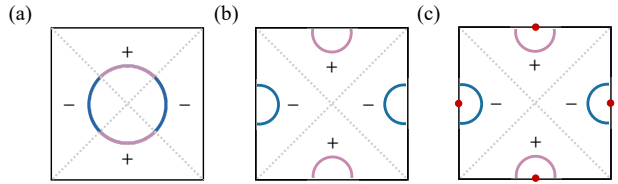


FIG. 1. Illustration of how the Fermi surface (solid lines) dictates superconducting properties for a d -wave pairing state. The dashed lines denote the pairing nodes. (a) Nodal phase. (b) Fully gapped phase with trivial topology. (c) Fully gapped phase with nontrivial topology, where the Fermi pockets enclose a Dirac point (red dots).

transition temperatures (T_c) [51–54]. In contrast, the most common pairing symmetries found in high- T_c materials, like the even-parity spin-singlet d -wave and extended s -wave observed in cuprates and iron-based systems [55–61], generally lead to nodal [Fig. 1(a)] or topologically trivial gapped states [Fig. 1(b)]. To achieve topological superconducting states from these even-parity, spin-singlet pairings with a fixed phase, the Fermi surface needs to enclose a band degeneracy so that it acquires nontrivial spin- or orbital-momentum locking [62, 63]. Furthermore, the pairing must change sign between different Fermi pockets [Fig. 1(c)], locking the nodes and the Fermi surface into a stable topological configuration that protects against adiabatic deformation to the trivial limit [64].

In this work, we explore intrinsic topological superconductivity in a two-dimensional, square-lattice nonsymmorphic Dirac semimetal (DSM) possessing \mathcal{PT} symmetry. The band structure features Dirac points at the time-reversal invariant momentums (TRIMs) $\mathbf{X} = (\pi, 0)$ and $\mathbf{Y} = (0, \pi)$, yielding two distinct Fermi pockets near half-filling, each enclosing one Dirac point. Using self-consistent mean-field theory for an on-site repulsive and nearest-neighbor attractive inter-

action, we find that the superconducting ground state favors an even-parity, spin-singlet $d_{x^2-y^2}$ -wave pairing. This pairing, which changes sign between the two pockets, results in a fully gapped phase identified as a second-order TSC. Notably, the resulting MZMs are highly tunable; unlike their typical pinning at sharp corners, their location along the edge can be engineered at will by controlling the boundary sublattice terminations.

DSM Hamiltonian.—We consider a DSM which consists of two layers that are relatively shifted by a vector $(1/2, 1/2)a$, where a denotes the lattice constant. From a top-down view, the bilayer forms a bipartite square lattice with primitive lattice vectors $\mathbf{a}_1 = \hat{a}\hat{x}$ and $\mathbf{a}_2 = a\hat{y}$, as illustrated in Fig. 2(a). The corresponding tight-binding Hamiltonian is given by

$$H_0 = - \sum_{\mathbf{r}, j, \alpha} \{ c_{\mathbf{r}, \alpha}^\dagger [t + i\lambda_{\text{so}}(\hat{\mathbf{a}}_j \times \mathbf{s})_z \xi_\alpha] c_{\mathbf{r}+\mathbf{a}_j, \alpha} + h.c. \} \\ + \sum_{\mathbf{r}, \beta} [\eta_\beta (c_{\mathbf{r}, A}^\dagger c_{\mathbf{r}+\delta_\beta, B} + c_{\mathbf{r}, A}^\dagger c_{\mathbf{r}-\delta_\beta, B}) + h.c.], \quad (1)$$

where \mathbf{r} denotes the Bravais lattice sites of either layer, specified by $\alpha = \{A, B\}$, $\hat{\mathbf{a}}_j = \mathbf{a}_j/a$ represents the unit vector along the j direction, and $c_{\mathbf{r}, \alpha}^\dagger \equiv (c_{\mathbf{r}, \alpha\uparrow}^\dagger, c_{\mathbf{r}, \alpha\downarrow}^\dagger)$ creates a fermion with spin s on the lattice \mathbf{r} of the layer α . The first line of the Hamiltonian describes the intra-layer nearest-neighbor hopping with amplitude t and the Rashba spin-orbit coupling of strength λ_{so} . The parameter ξ_α equals $+1$ for the top layer (A) and -1 for the bottom layer (B), indicating that the spin polarizations induced by the spin-orbit coupling are opposite in the two layers. The second line describes the interlayer nearest-neighbor hoppings along the two diagonal directions $\delta_\pm = \frac{1}{2}(-\mathbf{a}_1 \pm \mathbf{a}_2)$, with corresponding amplitudes $\eta_\pm = \eta_1 \pm \eta_2$ [see Fig. 2(a)]. It is worth pointing out that the particular form of spin-orbit coupling arises in systems where inversion symmetry is locally broken but globally preserved [65]. A representative example is the iron-based superconductor FeSe [66, 67]. Although the crystal as a whole is inversion-symmetric, the unit cell contains two inequivalent Fe atoms, each of which is asymmetrically coordinated by surrounding Se atoms, leading to a local breaking of inversion symmetry.

By performing a Fourier transformation from the real space to the momentum space, we obtain $H_0 = \sum_{\mathbf{k}} \psi_{\mathbf{k}}^\dagger \mathcal{H}(\mathbf{k}) \psi_{\mathbf{k}}$, where the basis function is $\psi_{\mathbf{k}}^\dagger = (c_{\mathbf{k}, A\uparrow}^\dagger, c_{\mathbf{k}, A\downarrow}^\dagger, c_{\mathbf{k}, B\uparrow}^\dagger, c_{\mathbf{k}, B\downarrow}^\dagger)$ and the momentum-space Hamiltonian is

$$\mathcal{H}(\mathbf{k}) = \epsilon(\mathbf{k}) + \eta(\mathbf{k})\sigma_x + 2\lambda_{\text{so}}\sigma_z(\sin k_x s_y - \sin k_y s_x). \quad (2)$$

Here we define the functions $\epsilon(\mathbf{k}) = -2t(\cos k_x + \cos k_y)$ and $\eta(\mathbf{k}) = 4[\eta_1 \cos(k_x/2) \cos(k_y/2) + \eta_2 \sin(k_x/2) \sin(k_y/2)]$ for brevity. The Pauli matrices σ_i and s_i act on the layer (A, B) and spin (\uparrow, \downarrow) space, respectively. For notational simplicity, we set the lattice constant a to unit and omit all identity matrices throughout the paper. This Hamiltonian possesses \mathcal{PT} symmetry ($\mathcal{PT} = \sigma_x s_y \mathcal{K}$ with \mathcal{K} the complex conjugation operator), and a glide symmetry ($\{\mathcal{M}_z|(\frac{1}{2}, \frac{1}{2})\} = i\sigma_x s_z$).

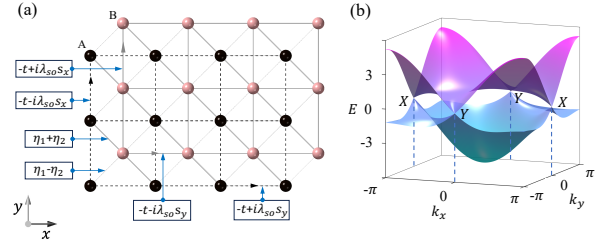


FIG. 2. (a) Sketch of a top-down view of the bilayer lattice, where the two layers are shifted by a vector $(1/2, 1/2)a$. The hopping and spin-orbit coupling coefficients are shown. (b) The band structure of the DSM, where the Dirac points appear at $\mathbf{X} = (\pi, 0)$, $\mathbf{Y} = (0, \pi)$. Parameters are $\{t, \lambda_{\text{so}}, \eta_1, \eta_2\} = \{0.5, 0.4, 0.8, 0.8\}$.

The latter symmetry operation consists of a mirror reflection about the middle plane of the two layers \mathcal{M}_z followed by a translation denoted by $(\frac{1}{2}, \frac{1}{2})$. When $\eta_2 = 0$, the Hamiltonian further possesses two screw symmetries, $\{\mathcal{C}_{2x}|(\frac{1}{2}, 0)\} = i\sigma_x s_x$ and $\{\mathcal{C}_{2y}|(0, \frac{1}{2})\} = i\sigma_x s_y$, where \mathcal{C}_{2a} denotes a π rotation about the a -axis [68, 69].

The coexistence of \mathcal{PT} symmetry and nonsymmorphic symmetry admits robust Dirac points in the band structure [68]. When $\eta_2 = 0$, there are three Dirac points, located at $\mathbf{X} = (\pi, 0)$, $\mathbf{Y} = (0, \pi)$ and $\mathbf{M} = (\pi, \pi)$. Once η_2 becomes finite, the Dirac point at \mathbf{M} is gapped, due to the breaking of the two screw symmetries. However, the two Dirac points at \mathbf{X} and \mathbf{Y} remain intact, as shown in Fig. 2(b). We focus on this general case which admits two well-separated, disconnected Fermi pockets, each enclosing a Dirac point.

The presence of Dirac points, which are momentum-space topological defects with singular quantum geometry, renders these Fermi pockets fundamentally distinct from conventional Fermi pockets that do not enclose them. We refer to the former as Dirac Fermi pockets (DFPs) and the latter normal Fermi pockets (NFPs). This distinction is underscored by a key topological constraint: a NFP can be continuously shrunk to a point and vanish under variation of system parameters (e.g., the chemical potential) without breaking any symmetry. In contrast, a DFP is topologically protected; it cannot vanish on its own and must instead annihilate in pairs with another DFP [70]. This inherent topological stability makes investigating the pairing symmetry in this system a subject of fundamental interest.

Pairing symmetry and spectrum.—We first classify the pairing channels based on symmetry. The momentum-space Hamiltonian possesses three crystal symmetries: inversion symmetry ($\mathcal{P}\mathcal{H}(\mathbf{k})\mathcal{P}^{-1} = \mathcal{H}(-\mathbf{k})$ with $\mathcal{P} = \sigma_x$), in-plane mirror symmetry ($\mathcal{M}_z \mathcal{H}(\mathbf{k}) \mathcal{M}_z^{-1} = \mathcal{H}(\mathbf{k})$ with $\mathcal{M}_z = i\sigma_x s_z$), and \mathcal{C}_{2z} rotation symmetry ($\mathcal{C}_{2z} \mathcal{H}(\mathbf{k}) \mathcal{C}_{2z}^{-1} = \mathcal{H}(-\mathbf{k})$ with $\mathcal{C}_{2z} = is_z$). Therefore, the pairing symmetry can be classified by the \mathcal{C}_{2h} group, which has four one-dimensional irreducible representations (IRs): two even-parity channels (A_g, B_g) and two odd-parity channels (A_u, B_u). Pairing in the A_g channel is conventionally classified as s -wave pairing because its order parameter is invariant under all symmetry operations

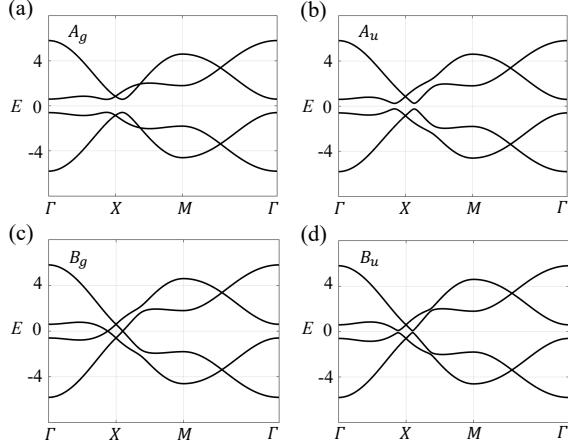


FIG. 3. BdG spectra corresponding to the pairing functions in the four different IRs. All spectra are calculated with the common parameter set: $\{t, \lambda_{\text{so}}, \eta_1, \eta_2, \mu, \Delta_{1x}, \Delta_{1y}\} = \{0.5, 0.4, 0.8, 0.8, 0.6, 0.3, -0.3\}$. For A_g and A_u , Δ_0 is set to zero. For B_g and B_u , we choose $M_\Delta = \tau_y \sigma_z s_x$ and $M'_\Delta = \tau_y s_x$, respectively.

of the group. However, its corresponding order parameter is not necessarily a constant.

Before considering specific interactions, we first outline the key characteristics of the superconducting states for the four IRs, including their energy spectra and topological properties. Since the pairings in these one-dimensional IRs preserve time-reversal symmetry, the resulting superconducting states all belong to symmetry class DIII [71–73]. Within this class, the first-order topology is characterized by a Z_2 invariant. As the inversion symmetry is also present, the Z_2 invariant can simply be defined as the product of parity eigenvalues of the negative-energy bands [74]. To facilitate a concrete analysis, we restrict the real-space pairing to nearest neighbors. This allows us to explicitly write down the general pairing function for each IR. In the Nambu basis, defined as $\Psi_k^\dagger = (\psi_k^\dagger, \psi_{-k}^T)$, the resulting pairing terms are as follows:

A_g : $(\Delta_0 + \Delta_{1x} \cos k_x + \Delta_{1y} \cos k_y) \tau_y s_y$, where τ_i are the Pauli matrices in particle-hole space. This even-parity, spin-singlet pairing leads a fully-gapped spectrum as long as the pairing nodes, if existing, do not cross the Fermi surface. In the gapped regime, the Z_2 invariant is always trivial, indicating that this pairing cannot give rise to first-order TSCs. However, as we will demonstrate later, this pairing can result in a second-order TSC, provided that the pairing nodes and the Fermi surface form a configuration similar to that in Fig. 1(c).

B_g : $(\Delta_{1x} \sin k_x + \Delta_{1y} \sin k_y) M_\Delta$, where $M_\Delta = \{\tau_y \sigma_z s_x, \tau_y \sigma_z s_z, \tau_x \sigma_z\}$. This channel corresponds to spin-triplet pairings. Because the pairing function vanishes identically at all TRIMs, the spectrum will always exhibit nodes. Therefore, this pairing channel gives rise to nodal superconducting phases.

A_u : $(\Delta_0 + \Delta_{1x} \cos k_x + \Delta_{1y} \cos k_y) \tau_y \sigma_z s_y$. This odd-parity, spin-singlet pairing produces a gapped spectrum un-

less a pairing node crosses the Fermi surface. Unlike the A_g case, this pairing can stabilize a first-order TSC phase. In the weak-pairing limit, the Z_2 invariant simplifies to a criterion based on the even or odd number of Fermi surfaces enclosing TRIMs [43, 44]. When there is a single Fermi surface, the Z_2 invariant is nontrivial, leading to a first-order TSC characterized by a pair of helical Majorana edge states [70].

B_u : $(\Delta_{1x} \sin k_x + \Delta_{1y} \sin k_y) M'_\Delta$, where $M'_\Delta = \{\tau_y s_x, \tau_y s_z, \tau_x\}$. Similar to the B_g case, the superconducting state always hosts a nodal spectrum. Therefore, this pairing channel also leads to nodal superconducting phases.

To qualitatively assess which pairing channel is energetically most stable, we compare the superconducting spectra for the four IRs under identical parameter conditions. Specifically, we consider a Fermi surface composed of two DFPs enclosing \mathbf{X} and \mathbf{Y} , respectively, and we set $\Delta_0 = 0$ and $\Delta_{1x} = -\Delta_{1y}$, as suggested by the solutions of the gap equation (see the following section). The calculated spectra along high-symmetry paths are shown in Fig. 3. Consistent with our theoretical analysis, the B_g and B_u pairings lead to a nodal spectrum, whereas the A_g and A_u pairings lead to a fully-gapped spectrum. Furthermore, the superconducting gap opened by the A_g pairing is noticeably larger than that of the A_u pairing. These spectral features suggest that the A_g channel is likely the leading pairing instability, a conclusion we will subsequently reinforce by analyzing a specific interaction.

Interaction and favored pairing.—We consider a short-range interaction:

$$H_{\text{int}} = U \sum_{i,\alpha} n_{i,\alpha\uparrow} n_{i,\alpha\downarrow} + V \sum_{<ij>,\alpha} n_{i,\alpha\uparrow} n_{j,\alpha\downarrow}, \quad (3)$$

where $U > 0$ is the strength of the on-site repulsive Hubbard interaction, and $V < 0$ is the strength of the attractive nearest-neighbor interaction within each layer ($\alpha = \{A, B\}$). The on-site repulsion U originates from the Coulomb interaction, while the attractive V can arise from electron-phonon coupling [75, 76] or other bosonic fluctuations. Here, we restrict the attractive nearest-neighbor interaction to electrons with opposite spin. While this interaction directly rules out spin-triplet pairings with total $S_z = \pm 1$, it still admits the one with $S_z = 0$. Therefore, this interaction is sufficient to generate pairing in all channels.

In momentum space the interaction reads

$$H_{\text{int}} = \frac{1}{N} \sum_{\mathbf{k}\mathbf{k}'\mathbf{q},\alpha} V(\mathbf{q}) c_{\mathbf{k}+\mathbf{q},\alpha\uparrow}^\dagger c_{\mathbf{k}'-\mathbf{q},\alpha\downarrow}^\dagger c_{\mathbf{k}',\alpha\downarrow} c_{\mathbf{k},\alpha\uparrow}, \quad (4)$$

where $V(\mathbf{q}) = U + 2V(\cos q_x + \cos q_y)$. We focus on zero-momentum pairings, for which the interaction can be simplified as

$$H_{\text{int}} \simeq \frac{1}{N} \sum_{\mathbf{k},\mathbf{k}',\alpha} V(\mathbf{k}-\mathbf{k}') c_{\mathbf{k},\alpha\uparrow}^\dagger c_{-\mathbf{k},\alpha\downarrow}^\dagger c_{-\mathbf{k}',\alpha\downarrow} c_{\mathbf{k}',\alpha\uparrow}. \quad (5)$$

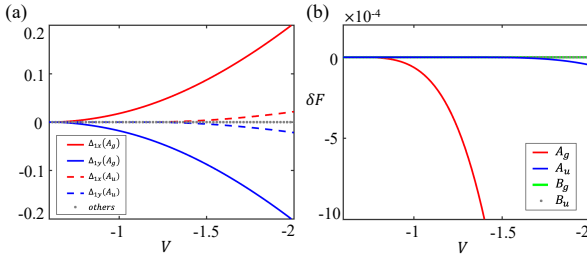


FIG. 4. (a) Pairing amplitudes for the gap functions in the four IRs. (b) Free-energy difference δF between the normal and superconducting states at zero temperature. Parameters are $\{t, \lambda_{\text{so}}, \eta_1, \eta_2, \mu, U\} = \{0.5, 0.4, 0.8, 0.8, 0.6, 0.1\}$.

Following the standard Bardeen-Cooper-Schrieffer (BCS) theory, we define the gap function as [77]

$$\Xi_{\alpha s, \alpha \bar{s}}(\mathbf{k}) = -\frac{1}{N} \sum_{\mathbf{k}'} V(\mathbf{k} - \mathbf{k}') \langle c_{\mathbf{k}', \alpha s} c_{-\mathbf{k}', \alpha \bar{s}} \rangle. \quad (6)$$

Since pairing occurs only within each layer, the gap function $\Xi(\mathbf{k})$ as a matrix is diagonal in the layer index. The Bogoliubov-de Gennes (BdG) mean-field Hamiltonian describing the superconducting state can be expressed as $H = \frac{1}{2} \sum_{\mathbf{k}} \Psi_{\mathbf{k}}^{\dagger} \mathcal{H}_{\text{BdG}}(\mathbf{k}) \Psi_{\mathbf{k}}$, with

$$\mathcal{H}_{\text{BdG}}(\mathbf{k}) = \begin{pmatrix} \mathcal{H}(\mathbf{k}) - \mu & \Xi(\mathbf{k}) \\ \Xi^{\dagger}(\mathbf{k}) & -\mathcal{H}^*(-\mathbf{k}) + \mu \end{pmatrix}. \quad (7)$$

Here, μ is the chemical potential, and $\Xi(\mathbf{k})$ is the pairing matrix. We employ a self-consistent procedure to determine the zero-temperature pairing amplitudes for each IR, iterating until convergence is reached. In our calculations, we set μ to a value where the Fermi surface contains two DFPs, fix the on-site repulsion U , and vary the nearest-neighbor attraction V to track the evolution of the pairing. As expected from the on-site repulsion, the numerical results show a vanishingly small on-site spin-singlet pairing amplitude Δ_0 . Furthermore, we find that $\Delta_{1x} = -\Delta_{1y}$ for all four pairing channels. Over the considered range of V , the B_g and B_u pairing amplitudes are negligible, while those of the A_u channel becomes notable for $V < -1.5$. In contrast, the A_g pairing amplitude is significantly larger than all others under the same conditions, as shown in Fig. 4(a). To identify the dominant superconducting channel, we compute the free energy difference $\delta F = F_S - F_N$ between the superconducting and normal states. The results in Fig. 4(b) clearly indicate that the A_g pairing channel is energetically favored, confirming it as the ground state.

Second-order TSC with tunable MZMs.— In this channel, the numerical results in Fig. 4(a) show that $\Delta_0 = 0$, and Δ_{1x} and Δ_{1y} take opposite values, resulting in a gap function of the form $\Xi(\mathbf{k}) = -i\Delta(\cos k_x - \cos k_y)s_y$ where $\Delta \equiv |\Delta_{1x}|$. While this functional form is characteristic of a $d_{x^2-y^2}$ -wave pairing, the C_{2h} symmetry group of the system does not distinguish it from a conventional s -wave pairing, both belonging to the A_g IR. This is evidenced by the gap function having

a fixed sign on each DFP, similar to the behavior of the gap function in a conventional s -wave superconductor. The key physical distinction, however, is that this gap function has opposite signs on the two DFPs located near the \mathbf{X} and \mathbf{Y} points. As we demonstrate below, this sign structure directly leads to a second-order TSC with tunable MZMs.

The BdG Hamiltonian commutes with the mirror symmetry operator, $[\mathcal{H}_{\text{BdG}}(\mathbf{k}), \tilde{\mathcal{M}}_z] = 0$, where $\tilde{\mathcal{M}}_z = i\tau_z \sigma_x s_z$. Since $\tilde{\mathcal{M}}_z$ has eigenvalues $\pm i$, the Hamiltonian can be block-diagonalized as $\mathcal{H}_{\text{BdG}} = \mathcal{H}_{+i} \oplus \mathcal{H}_{-i}$, corresponding to the two mirror subsectors. In the basis where $\tilde{\mathcal{M}}_z$ is diagonal, we have

$$\begin{aligned} \mathcal{H}_{\pm i}(\mathbf{k}) = & (\epsilon(\mathbf{k}) - \mu)\tau_z + \eta(\mathbf{k})\tau_z\rho_z \mp \Delta(\mathbf{k})\tau_x\rho_x \\ & + 2\lambda_{\text{so}}(\mp \sin k_x \rho_y + \sin k_y \rho_x), \end{aligned} \quad (8)$$

where we define $\Delta(\mathbf{k}) = \Delta(\cos k_x - \cos k_y)$, and $\rho_{x,y,z}$ are Pauli matrices acting on the two-dimensional Hilbert space spanned by the eigenvectors of $\sigma_x s_z$ with positive or negative eigenvalues. Each mirror sector of the Hamiltonian possesses chiral symmetry, represented by the operator $S = \tau_y \rho_z$, and therefore belongs to the AIII class. This symmetry class does not support first-order topological gapped phases in two dimensions [71–73]. Nevertheless, we find that each sector is characterized by a nontrivial quantized quadrupole moment $q_{xy} = 1/2$ [78–82], indicating a second-order topological phase. Further confirmation comes from diagonalizing the full Hamiltonian under open boundary conditions along both the x and y directions. Consistent with the bulk topological invariant, our computation reveals the presence of eight MZMs, localized as a Kramers pair at each corner, as shown in Fig. 5(a). This explicitly demonstrates the system as a second-order TSC.

Remarkably, unlike typical second-order TSCs where MZMs are pinned at sharp corners [83–115], our system allows precise control over the number and spatial locations of MZMs simply by tailoring the edge termination, as shown in Figs. 5(b) and 5(c). This tunability arises from a dimerized hopping structure in the Hamiltonian when both η_1 and η_2 are non-zero, which makes the boundary topology highly sensitive to the sublattice (or layer) termination [116, 117]. Although such sublattice-dependent MZMs were previously predicted in heterostructures combining topological insulators and superconductors [118–120], here we demonstrate for the first time that this phenomenon can be realized in an intrinsic second-order TSC.

Discussions and conclusions.—The connection between opposite-sign pairing on DFPs and second-order topology was previously noted by Qin *et al.* [66], whose scenario involves two concentric DFPs and an extended s -wave pairing with nodes between them. Here, starting from an interacting Hamiltonian, we show that the superconducting ground state with $d_{x^2-y^2}$ -wave order parameter also leads to the same physics, even though the DFPs in our case enclose distinct Dirac points. This suggests the generality of the underlying principle and allows us to formulate a universal topological

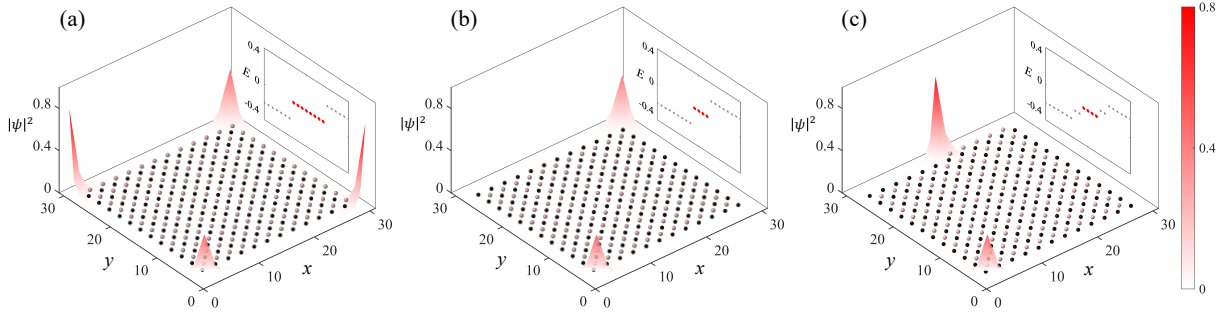


FIG. 5. Tunability of MZMs via sublattice termination. (a) With complete unit cells at all boundaries, the system hosts one Majorana Kramers pair at each corner. (b) Changing the sublattice termination on the upper (y -normal) and right (x -normal) edges halves the number of Majorana Kramers pairs. (c) Further adjusting the termination of the upper edge creates a domain wall and relocates a Majorana Kramers pair from the corner to a generic boundary site. The MZM count is quantified by the number of zero-energy states shown in the insets. Common parameters: $\{t, \lambda_{\text{so}}, \eta_1, \eta_2, \mu, \Delta\} = \{0.5, 0.4, 0.8, 0.8, 0.6, 0.3\}$

criterion: $(-1)^\nu = \prod_n \text{sgn}(\Delta)_n$, where $\nu = 1$ (0) denotes the topological (trivial) phase and $\text{sgn}(\Delta)_n$ is the pairing sign on the n th DFP. Furthermore, we identify a novel tunability: the MZMs in our system can be repositioned by modifying the boundary termination, a feature not explored in the prior work.

To conclude, we have shown that intrinsic topological superconductivity can arise in DSMs from interaction-driven, even-parity spin-singlet pairing. The established mechanism can be directly generalized to three-dimensional nonsymmorphic DSMs [121–124]. Drawing parallels with high- T_c cuprates, our proposed d -wave second-order TSC may potentially be stabilized at elevated temperatures, providing a promising platform for MZMs that benefits from a large pairing gap and low disorder. Furthermore, the unique combination of d -wave pairing and Dirac Fermi surfaces in this phase should give rise to additional novel physics; for instance, the vortex properties are anticipated to differ significantly from those in conventional gapless d -wave superconductors [125–127]. Given the abundance of DSM materials [128–134], our simple topological criterion provides a clear guideline for screening candidates with the requisite Fermi surface configuration and superconductivity. Lastly, cold-atom systems, with their exceptional tunability, present an ideal alternative platform for implementing our proposed scenario.

Acknowledgements.—This work is supported by the National Natural Science Foundation of China (Grant No. 12174455, No. 12474264, No. 12174453, No. 12574153), Guangdong Basic and Applied Basic Research Foundation (Grant No. 2023B1515040023), Guangdong Provincial Quantum Science Strategic Initiative (Grant No. GDZX2404007) and National Key R&D Program of China (Grant No. 2022YFA1404103).

- [1] X.-L. Qi and S.-C. Zhang, Topological insulators and superconductors, *Rev. Mod. Phys.* **83**, 1057 (2011).
- [2] J. Alicea, New directions in the pursuit of majorana fermions in solid state systems, *Reports on Progress in Physics* **75**, 076501 (2012).
- [3] M. Leijnse and K. Flensberg, Introduction to topological superconductivity and majorana fermions, *Semiconductor Science and Technology* **27**, 124003 (2012).
- [4] Y. Tanaka, M. Sato, and N. Nagaosa, Symmetry and Topology in Superconductors—Odd-Frequency Pairing and Edge States—, *Journal of the Physical Society of Japan* **81**, 011013 (2012).
- [5] T. D. Stanescu and S. Tewari, Majorana fermions in semiconductor nanowires: fundamentals, modeling, and experiment, *Journal of Physics: Condensed Matter* **25**, 233201 (2013).
- [6] C. W. J. Beenakker, Search for Majorana Fermions in Superconductors, *Annual Review of Condensed Matter Physics* **4**, 113 (2013).
- [7] S. R. Elliott and M. Franz, *Colloquium* : Majorana fermions in nuclear, particle, and solid-state physics, *Rev. Mod. Phys.* **87**, 137 (2015).
- [8] M. Sato and S. Fujimoto, Majorana Fermions and Topology in Superconductors, *Journal of the Physical Society of Japan* **85**, 072001 (2016).
- [9] C. Nayak, S. H. Simon, A. Stern, M. Freedman, and S. Das Sarma, Non-Abelian anyons and topological quantum computation, *Rev. Mod. Phys.* **80**, 1083 (2008).
- [10] S. D. Sarma, M. Freedman, and C. Nayak, Majorana zero modes and topological quantum computation, *npj Quantum Information* **1**, 15001 (2015).
- [11] T. Karzig, C. Knapp, R. M. Lutchyn, P. Bonderson, M. B. Hastings, C. Nayak, J. Alicea, K. Flensberg, S. Plugge, Y. Oreg, C. M. Marcus, and M. H. Freedman, Scalable designs for quasiparticle-poisoning-protected topological quantum computation with Majorana zero modes, *Phys. Rev. B* **95**, 235305 (2017).
- [12] P. Marra, Majorana nanowires for topological quantum computation, *Journal of Applied Physics* **132**, 231101 (2022).
- [13] N. Read and D. Green, Paired states of fermions in two dimensions with breaking of parity and time-reversal symmetries and the fractional quantum Hall effect, *Phys. Rev. B* **61**, 10267 (2000).
- [14] A. Y. Kitaev, Unpaired majorana fermions in quantum wires, *Physics-Uspekhi* **44**, 131 (2001).
- [15] L. Fu and C. L. Kane, Superconducting Proximity Effect and

* wuzhigang@quantumsc.cn
† yanzhb5@mail.sysu.edu.cn

- Majorana Fermions at the Surface of a Topological Insulator, Phys. Rev. Lett. **100**, 096407 (2008).
- [16] M. Sato, Y. Takahashi, and S. Fujimoto, Non-Abelian Topological Order in *s*-Wave Superfluids of Ultracold Fermionic Atoms, Phys. Rev. Lett. **103**, 020401 (2009).
- [17] R. M. Lutchyn, J. D. Sau, and S. Das Sarma, Majorana Fermions and a Topological Phase Transition in Semiconductor-Superconductor Heterostructures, Phys. Rev. Lett. **105**, 077001 (2010).
- [18] Y. Oreg, G. Refael, and F. von Oppen, Helical Liquids and Majorana Bound States in Quantum Wires, Phys. Rev. Lett. **105**, 177002 (2010).
- [19] J. Alicea, Majorana fermions in a tunable semiconductor device, Phys. Rev. B **81**, 125318 (2010).
- [20] J.-P. Xu, M.-X. Wang, Z. L. Liu, J.-F. Ge, X. Yang, C. Liu, Z. A. Xu, D. Guan, C. L. Gao, D. Qian, Y. Liu, Q.-H. Wang, F.-C. Zhang, Q.-K. Xue, and J.-F. Jia, Experimental Detection of a Majorana Mode in the core of a Magnetic Vortex inside a Topological Insulator-Superconductor $\text{Bi}_2\text{Te}_3/\text{NbSe}_2$ Heterostructure, Phys. Rev. Lett. **114**, 017001 (2015).
- [21] H.-H. Sun, K.-W. Zhang, L.-H. Hu, C. Li, G.-Y. Wang, H.-Y. Ma, Z.-A. Xu, C.-L. Gao, D.-D. Guan, Y.-Y. Li, C. Liu, D. Qian, Y. Zhou, L. Fu, S.-C. Li, F.-C. Zhang, and J.-F. Jia, Majorana Zero Mode Detected with Spin Selective Andreev Reflection in the Vortex of a Topological Superconductor, Phys. Rev. Lett. **116**, 257003 (2016).
- [22] T. Liu, C. Y. Wan, H. Yang, Y. Zhao, B. Xie, W. Zheng, Z. Yi, D. Guan, S. Wang, H. Zheng, C. Liu, L. Fu, J. Liu, Y. Li, and J. Jia, Signatures of hybridization of multiple Majorana zero modes in a vortex, Nature **633**, 71 (2024).
- [23] S. Nadj-Perge, I. K. Drozdov, J. Li, H. Chen, S. Jeon, J. Seo, A. H. MacDonald, B. A. Bernevig, and A. Yazdani, Observation of Majorana fermions in ferromagnetic atomic chains on a superconductor, Science **346**, 602 (2014).
- [24] S. Jeon, Y. Xie, J. Li, Z. Wang, B. A. Bernevig, and A. Yazdani, Distinguishing a Majorana zero mode using spin-resolved measurements, Science **358**, 772 (2017).
- [25] V. Mourik, K. Zuo, S. M. Frolov, S. R. Plissard, E. P. A. M. Bakkers, and L. P. Kouwenhoven, Signatures of Majorana Fermions in Hybrid Superconductor-Semiconductor Nanowire Devices, Science **336**, 1003 (2012).
- [26] A. Das, Y. Ronen, Y. Most, Y. Oreg, M. Heiblum, and H. Shtrikman, Zero-bias peaks and splitting in an Al-InAs nanowire topological superconductor as a signature of Majorana fermions, Nature Physics **8**, 887 (2012).
- [27] M. T. Deng, C. L. Yu, G. Y. Huang, M. Larsson, P. Caroff, and H. Q. Xu, Anomalous Zero-Bias Conductance Peak in a Nb-InSb Nanowire-Nb Hybrid Device, Nano Letters **12**, 6414 (2012).
- [28] A. D. K. Finck, D. J. Van Harlingen, P. K. Mohseni, K. Jung, and X. Li, Anomalous modulation of a zero-bias peak in a hybrid nanowire-superconductor device, Phys. Rev. Lett. **110**, 126406 (2013).
- [29] E. Prada, P. San-Jose, M. W. A. de Moor, A. Geresdi, E. J. H. Lee, J. Klinovaja, D. Loss, J. Nygård, R. Aguado, and L. P. Kouwenhoven, From andreev to majorana bound states in hybrid superconductor-semiconductor nanowires, Nature Reviews Physics **2**, 575 (2020).
- [30] K. Flensberg, F. von Oppen, and A. Stern, Engineered platforms for topological superconductivity and majorana zero modes, Nature Reviews Materials **6**, 944 (2021).
- [31] S. Das Sarma and H. Pan, Disorder-induced zero-bias peaks in Majorana nanowires, Phys. Rev. B **103**, 195158 (2021).
- [32] A. Yazdani, F. von Oppen, B. I. Halperin, and A. Yacoby, Hunting for majoranas, Science **380**, eade0850 (2023).
- [33] Z. Wang, P. Zhang, G. Xu, L. K. Zeng, H. Miao, X. Xu, T. Qian, H. Weng, P. Richard, A. V. Fedorov, H. Ding, X. Dai, and Z. Fang, Topological nature of the $\text{FeSe}_{0.5}\text{Te}_{0.5}$ superconductor, Phys. Rev. B **92**, 115119 (2015).
- [34] G. Xu, B. Lian, P. Tang, X.-L. Qi, and S.-C. Zhang, Topological superconductivity on the surface of fe-based superconductors, Phys. Rev. Lett. **117**, 047001 (2016).
- [35] P. Zhang, K. Yaji, T. Hashimoto, Y. Ota, T. Kondo, K. Okazaki, Z. Wang, J. Wen, G. Gu, H. Ding, et al., Observation of topological superconductivity on the surface of an iron-based superconductor, Science **360**, 182 (2018).
- [36] R.-X. Zhang, W. S. Cole, and S. Das Sarma, Helical hinge Majorana modes in iron-based superconductors, Phys. Rev. Lett. **122**, 187001 (2019).
- [37] M. Kheirkhah, Z.-Y. Zhuang, J. Maciejko, and Z. Yan, Surface Bogoliubov-Dirac cones and helical Majorana hinge modes in superconducting Dirac semimetals, Phys. Rev. B **105**, 014509 (2022).
- [38] D. Wang, L. Kong, P. Fan, H. Chen, S. Zhu, W. Liu, L. Cao, Y. Sun, S. Du, J. Schneeloch, et al., Evidence for Majorana bound states in an iron-based superconductor, Science **362**, 333 (2018).
- [39] Q. Liu, C. Chen, T. Zhang, R. Peng, Y.-J. Yan, C.-H.-P. Wen, X. Lou, Y.-L. Huang, J.-P. Tian, X.-L. Dong, G.-W. Wang, W.-C. Bao, Q.-H. Wang, Z.-P. Yin, Z.-X. Zhao, and D.-L. Feng, Robust and clean majorana zero mode in the vortex core of high-temperature superconductor $(\text{Li}_{0.84}\text{Fe}_{0.16})\text{OHFeSe}$, Phys. Rev. X **8**, 041056 (2018).
- [40] T. Machida, Y. Sun, S. Pyon, S. Takeda, Y. Kohsaka, T. Hanaguri, T. Sasagawa, and T. Tamegai, Zero-energy vortex bound state in the superconducting topological surface state of Fe (Se, Te), Nature materials , 1 (2019).
- [41] L. Kong, S. Zhu, M. Papaj, H. Chen, L. Cao, H. Isobe, Y. Xing, W. Liu, D. Wang, P. Fan, et al., Half-integer level shift of vortex bound states in an iron-based superconductor, Nature Physics , 1 (2019).
- [42] X.-L. Qi, T. L. Hughes, and S.-C. Zhang, Topological invariants for the Fermi surface of a time-reversal-invariant superconductor, Phys. Rev. B **81**, 134508 (2010).
- [43] M. Sato, Topological odd-parity superconductors, Phys. Rev. B **81**, 220504 (2010).
- [44] L. Fu and E. Berg, Odd-Parity Topological Superconductors: Theory and Application to $\text{Cu}_x\text{Bi}_2\text{Se}_3$, Phys. Rev. Lett. **105**, 097001 (2010).
- [45] X.-L. Qi, T. L. Hughes, S. Raghu, and S.-C. Zhang, Time-Reversal-Invariant Topological Superconductors and Superfluids in Two and Three Dimensions, Phys. Rev. Lett. **102**, 187001 (2009).
- [46] A. M. Black-Schaffer, Edge Properties and Majorana Fermions in the Proposed Chiral *d*-Wave Superconducting State of Doped Graphene, Phys. Rev. Lett. **109**, 197001 (2012).
- [47] F. Liu, C.-C. Liu, K. Wu, F. Yang, and Y. Yao, $d + id'$ Chiral Superconductivity in Bilayer Silicene, Phys. Rev. Lett. **111**, 066804 (2013).
- [48] W. Qin, L. Li, and Z. Zhang, Chiral topological superconductivity arising from the interplay of geometric phase and electron correlation, Nature Physics **15**, 796 (2019).
- [49] H. D. Scammell, J. Ingham, M. Geier, and T. Li, Intrinsic first- and higher-order topological superconductivity in a doped topological insulator, Phys. Rev. B **105**, 195149 (2022).
- [50] A. Jahin and Y. Wang, Higher-order topological superconduc-

- tivity in monolayer WTe₂ from repulsive interactions, Phys. Rev. B **108**, 014509 (2023).
- [51] S. S. Saxena, P. Agarwal, K. Ahilan, F. M. Grosche, R. K. W. Haselwimmer, M. J. Steiner, E. Pugh, I. R. Walker, S. R. Julian, P. Monthoux, G. G. Lonzarich, A. Huxley, I. Sheikin, D. Braithwaite, and J. Flouquet, Superconductivity on the border of itinerant-electron ferromagnetism in UGe₂, Nature **406**, 587 (2000).
- [52] D. Aoki, A. Huxley, E. Ressouche, D. Braithwaite, J. Flouquet, J.-P. Brison, E. Lhotel, and C. Paulsen, Coexistence of superconductivity and ferromagnetism in URhGe, Nature **413**, 613 (2001).
- [53] N. T. Huy, A. Gasparini, D. E. de Nijs, Y. Huang, J. C. P. Klaasse, T. Gortenmulder, A. de Visser, A. Hamann, T. Görlach, and H. v. Löhneysen, Superconductivity on the Border of Weak Itinerant Ferromagnetism in UCoGe, Phys. Rev. Lett. **99**, 067006 (2007).
- [54] S. Ran, C. Eckberg, Q.-P. Ding, Y. Furukawa, T. Metz, S. R. Saha, I.-L. Liu, M. Zic, H. Kim, J. Paglione, and N. P. Butch, Nearly ferromagnetic spin-triplet superconductivity, Science **365**, 684 (2019).
- [55] D. J. Van Harlingen, Phase-sensitive tests of the symmetry of the pairing state in the high-temperature superconductors—Evidence for $d_{x^2-y^2}$ symmetry, Rev. Mod. Phys. **67**, 515 (1995).
- [56] C. C. Tsuei and J. R. Kirtley, Pairing symmetry in cuprate superconductors, Rev. Mod. Phys. **72**, 969 (2000).
- [57] A. Damascelli, Z. Hussain, and Z.-X. Shen, Angle-resolved photoemission studies of the cuprate superconductors, Rev. Mod. Phys. **75**, 473 (2003).
- [58] J. Paglione and R. L. Greene, High-temperature superconductivity in iron-based materials, Nature Physics **6**, 645 (2010).
- [59] F. Wang and D.-H. Lee, The Electron-Pairing Mechanism of Iron-Based Superconductors, Science **332**, 200 (2011).
- [60] P. J. Hirschfeld, M. M. Korshunov, and I. I. Mazin, Gap symmetry and structure of Fe-based superconductors, Reports on Progress in Physics **74**, 124508 (2011).
- [61] A. Chubukov, Pairing mechanism in fe-based superconductors, Annual Review of Condensed Matter Physics **3**, 57 (2012).
- [62] F. Zhang, C. L. Kane, and E. J. Mele, Time-Reversal-Invariant Topological Superconductivity and Majorana Kramers Pairs, Phys. Rev. Lett. **111**, 056402 (2013).
- [63] P. Hosur, X. Dai, Z. Fang, and X.-L. Qi, Time-reversal-invariant topological superconductivity in doped Weyl semimetals, Phys. Rev. B **90**, 045130 (2014).
- [64] Z. Yan, Unconventional topological insulators from extended topological band degeneracies, Phys. Rev. B **102**, 115151 (2020).
- [65] X. Zhang, Q. Liu, J.-W. Luo, A. J. Freeman, and A. Zunger, Hidden spin polarization in inversion-symmetric bulk crystals, Nature Physics **10**, 387 (2014).
- [66] S. Qin, C. Fang, F.-C. Zhang, and J. Hu, Topological Superconductivity in an Extended *s*-Wave Superconductor and Its Implication to Iron-Based Superconductors, Phys. Rev. X **12**, 011030 (2022).
- [67] Z. Zhang, Z. Wu, C. Fang, F.-c. Zhang, J. Hu, Y. Wang, and S. Qin, Topological superconductivity from unconventional band degeneracy with conventional pairing, Nature Communications **15**, 7971 (2024).
- [68] S. M. Young and C. L. Kane, Dirac Semimetals in Two Dimensions, Phys. Rev. Lett. **115**, 126803 (2015).
- [69] Y. Mo, X.-J. Wang, Z.-Y. Zhuang, and Z. Yan, Coexistence of chiral Majorana edge states and Bogoliubov Fermi surfaces in two-dimensional nonsymmorphic Dirac semimetal/superconductor heterostructures, Phys. Rev. B **111**, L140504 (2025).
- [70] Y. Mo, X.-J. Wang, and Z. Yan, Topological superconductivity in two-dimensional π -junction Dirac semimetals, Phys. Rev. B **112**, 115421 (2025).
- [71] A. P. Schnyder, S. Ryu, A. Furusaki, and A. W. W. Ludwig, Classification of topological insulators and superconductors in three spatial dimensions, Phys. Rev. B **78**, 195125 (2008).
- [72] A. Kitaev, Periodic table for topological insulators and superconductors, AIP conference proceedings, **1134**, 22 (2009).
- [73] S. Ryu, A. P. Schnyder, A. Furusaki, and A. W. W. Ludwig, Topological insulators and superconductors: tenfold way and dimensional hierarchy, New Journal of Physics **12**, 065010 (2010).
- [74] L. Fu and C. L. Kane, Topological insulators with inversion symmetry, Phys. Rev. B **76**, 045302 (2007).
- [75] Z. Chen, Y. Wang, S. N. Rebec, T. Jia, M. Hashimoto, D. Lu, B. Moritz, R. G. Moore, T. P. Devereaux, and Z.-X. Shen, Anomalously strong near-neighbor attraction in doped 1D cuprate chains, Science **373**, 1235 (2021).
- [76] C. Peng, Y. Wang, J. Wen, Y. S. Lee, T. P. Devereaux, and H.-C. Jiang, Enhanced superconductivity by near-neighbor attraction in the doped extended Hubbard model, Phys. Rev. B **107**, L201102 (2023).
- [77] D. Zhu, Z.-Y. Zhuang, Z. Wu, and Z. Yan, Topological superconductivity in two-dimensional altermagnetic metals, Phys. Rev. B **108**, 184505 (2023).
- [78] W. A. Benalcazar, B. A. Bernevig, and T. L. Hughes, Quantized electric multipole insulators, Science **357**, 61 (2017).
- [79] W. A. Benalcazar, B. A. Bernevig, and T. L. Hughes, Electric multipole moments, topological multipole moment pumping, and chiral hinge states in crystalline insulators, Phys. Rev. B **96**, 245115 (2017).
- [80] B. Kang, K. Shiozaki, and G. Y. Cho, Many-body order parameters for multipoles in solids, Phys. Rev. B **100**, 245134 (2019).
- [81] Y.-B. Yang, K. Li, L.-M. Duan, and Y. Xu, Higher-order topological Anderson insulators, Phys. Rev. B **103**, 085408 (2021).
- [82] C.-A. Li, B. Fu, Z.-A. Hu, J. Li, and S.-Q. Shen, Topological Phase Transitions in Disordered Electric Quadrupole Insulators, Phys. Rev. Lett. **125**, 166801 (2020).
- [83] J. Langbehn, Y. Peng, L. Trifunovic, F. von Oppen, and P. W. Brouwer, Reflection-Symmetric Second-Order Topological Insulators and Superconductors, Phys. Rev. Lett. **119**, 246401 (2017).
- [84] M. Geier, L. Trifunovic, M. Hoskam, and P. W. Brouwer, Second-order topological insulators and superconductors with an order-two crystalline symmetry, Phys. Rev. B **97**, 205135 (2018).
- [85] E. Khalaf, Higher-order topological insulators and superconductors protected by inversion symmetry, Phys. Rev. B **97**, 205136 (2018).
- [86] X. Zhu, Tunable Majorana corner states in a two-dimensional second-order topological superconductor induced by magnetic fields, Phys. Rev. B **97**, 205134 (2018).
- [87] Z. Yan, F. Song, and Z. Wang, Majorana Corner Modes in a High-Temperature Platform, Phys. Rev. Lett. **121**, 096803 (2018).
- [88] Y. Wang, M. Lin, and T. L. Hughes, Weak-pairing higher order topological superconductors, Phys. Rev. B **98**, 165144 (2018).
- [89] Q. Wang, C.-C. Liu, Y.-M. Lu, and F. Zhang, High-Temperature Majorana Corner States, Phys. Rev. Lett. **121**, 186801 (2018).

- [90] T. Liu, J. J. He, and F. Nori, Majorana corner states in a two-dimensional magnetic topological insulator on a high-temperature superconductor, *Phys. Rev. B* **98**, 245413 (2018).
- [91] C.-H. Hsu, P. Stano, J. Klinovaja, and D. Loss, Majorana kramers pairs in higher-order topological insulators, *Phys. Rev. Lett.* **121**, 196801 (2018).
- [92] Z. Wu, Z. Yan, and W. Huang, Higher-order topological superconductivity: Possible realization in Fermi gases and Sr_2RuO_4 , *Phys. Rev. B* **99**, 020508 (2019).
- [93] Z. Yan, Higher-Order Topological Odd-Parity Superconductors, *Phys. Rev. Lett.* **123**, 177001 (2019).
- [94] Z. Yan, Majorana corner and hinge modes in second-order topological insulator/superconductor heterostructures, *Phys. Rev. B* **100**, 205406 (2019).
- [95] Y. Volpez, D. Loss, and J. Klinovaja, Second-Order Topological Superconductivity in π -Junction Rashba Layers, *Phys. Rev. Lett.* **122**, 126402 (2019).
- [96] R.-X. Zhang, W. S. Cole, X. Wu, and S. Das Sarma, Higher-Order Topology and Nodal Topological Superconductivity in $\text{Fe}(\text{Se},\text{Te})$ Heterostructures, *Phys. Rev. Lett.* **123**, 167001 (2019).
- [97] X.-H. Pan, K.-J. Yang, L. Chen, G. Xu, C.-X. Liu, and X. Liu, Lattice-Symmetry-Assisted Second-Order Topological Superconductors and Majorana Patterns, *Phys. Rev. Lett.* **123**, 156801 (2019).
- [98] X. Zhu, Second-Order Topological Superconductors with Mixed Pairing, *Phys. Rev. Lett.* **122**, 236401 (2019).
- [99] J. Ahn and B.-J. Yang, Higher-order topological superconductivity of spin-polarized fermions, *Phys. Rev. Research* **2**, 012060 (2020).
- [100] Y.-T. Hsu, W. S. Cole, R.-X. Zhang, and J. D. Sau, Inversion-Protected Higher-Order Topological Superconductivity in Monolayer WTe_2 , *Phys. Rev. Lett.* **125**, 097001 (2020).
- [101] Y.-J. Wu, J. Hou, Y.-M. Li, X.-W. Luo, X. Shi, and C. Zhang, In-Plane Zeeman-Field-Induced Majorana Corner and Hinge Modes in an *s*-Wave Superconductor Heterostructure, *Phys. Rev. Lett.* **124**, 227001 (2020).
- [102] M. Kheirkhah, Z. Yan, Y. Nagai, and F. Marsiglio, First- and Second-Order Topological Superconductivity and Temperature-Driven Topological Phase Transitions in the Extended Hubbard Model with Spin-Orbit Coupling, *Phys. Rev. Lett.* **125**, 017001 (2020).
- [103] S. Franca, D. V. Efremov, and I. C. Fulga, Phase-tunable second-order topological superconductor, *Phys. Rev. B* **100**, 075415 (2019).
- [104] X. Wu, W. A. Benalcazar, Y. Li, R. Thomale, C.-X. Liu, and J. Hu, Boundary-Obstructed Topological High- T_c Superconductivity in Iron Pnictides, *Phys. Rev. X* **10**, 041014 (2020).
- [105] K. Laubscher, D. Chughtai, D. Loss, and J. Klinovaja, Kramers pairs of Majorana corner states in a topological insulator bilayer, *Phys. Rev. B* **102**, 195401 (2020).
- [106] B. Roy, Higher-order topological superconductors in \mathcal{P} -, \mathcal{T} -odd quadrupolar Dirac materials, *Phys. Rev. B* **101**, 220506 (2020).
- [107] B.-X. Li and Z. Yan, Boundary topological superconductors, *Phys. Rev. B* **103**, 064512 (2021).
- [108] X.-J. Luo, X.-H. Pan, and X. Liu, Higher-order topological superconductors based on weak topological insulators, *Phys. Rev. B* **104**, 104510 (2021).
- [109] A. K. Ghosh, T. Nag, and A. Saha, Hierarchy of higher-order topological superconductors in three dimensions, *Phys. Rev. B* **104**, 134508 (2021).
- [110] Y.-X. Li and C.-C. Liu, Majorana corner modes and tunable patterns in an altermagnet heterostructure, *Phys. Rev. B* **108**, 205410 (2023).
- [111] S. A. A. Ghorashi, T. L. Hughes, and J. Cano, Altermagnetic Routes to Majorana Modes in Zero Net Magnetization, *Phys. Rev. Lett.* **133**, 106601 (2024).
- [112] P. Chatterjee, A. K. Ghosh, A. K. Nandy, and A. Saha, Second-order topological superconductor via noncollinear magnetic texture, *Phys. Rev. B* **109**, L041409 (2024).
- [113] P. M. Bonetti, D. Chakraborty, X. Wu, and A. P. Schnyder, Interaction-driven first-order and higher-order topological superconductivity, *Phys. Rev. B* **109**, L180509 (2024).
- [114] H.-Y. Sun, L. Liu, Y.-T. Zhang, and Z. Qiao, Altermagnetism-induced iron-based third-order topological superconductivity, *Phys. Rev. B* **112**, 195402 (2025).
- [115] L. Liu, C. Miao, H. Tang, Y.-T. Zhang, and Z. Qiao, Magnetically controlled topological braiding with majorana corner states in second-order topological superconductors, *Phys. Rev. B* **109**, 115413 (2024).
- [116] The supplemental material contains the details of: (I) Topological configuration in momentum space and second-order topology; (II) Bulk topological invariant; (III) Edge-state theory for tunable MZMs.
- [117] J. C. Y. Teo and C. L. Kane, Topological defects and gapless modes in insulators and superconductors, *Phys. Rev. B* **82**, 115120 (2010).
- [118] D. Zhu, B.-X. Li, and Z. Yan, Sublattice-sensitive Majorana modes, *Phys. Rev. B* **106**, 245418 (2022).
- [119] D. Zhu, M. Kheirkhah, and Z. Yan, Sublattice-enriched tunability of bound states in second-order topological insulators and superconductors, *Phys. Rev. B* **107**, 085407 (2023).
- [120] M. Kheirkhah, D. Zhu, J. Maciejko, and Z. Yan, Corner- and sublattice-sensitive Majorana zero modes on the kagome lattice, *Phys. Rev. B* **106**, 085420 (2022).
- [121] S. M. Young, S. Zaheer, J. C. Y. Teo, C. L. Kane, E. J. Mele, and A. M. Rappe, Dirac semimetal in three dimensions, *Phys. Rev. Lett.* **108**, 140405 (2012).
- [122] J. A. Steinberg, S. M. Young, S. Zaheer, C. L. Kane, E. J. Mele, and A. M. Rappe, Bulk Dirac Points in Distorted Spinels, *Phys. Rev. Lett.* **112**, 036403 (2014).
- [123] Q. D. Gibson, L. M. Schoop, L. Muechler, L. S. Xie, M. Hirschberger, N. P. Ong, R. Car, and R. J. Cava, Three-dimensional Dirac semimetals: Design principles and predictions of new materials, *Phys. Rev. B* **91**, 205128 (2015).
- [124] B. J. Wieder, Y. Kim, A. M. Rappe, and C. L. Kane, Double dirac semimetals in three dimensions, *Phys. Rev. Lett.* **116**, 186402 (2016).
- [125] P. I. Soininen, C. Kallin, and A. J. Berlinsky, Structure of a vortex line in a $d_{x^2-y^2}$ superconductor, *Phys. Rev. B* **50**, 13883 (1994).
- [126] M. Ichioka, N. Hayashi, N. Enomoto, and K. Machida, Vortex structure in d-wave superconductors, *Phys. Rev. B* **53**, 15316 (1996).
- [127] M. Franz, C. Kallin, P. I. Soininen, A. J. Berlinsky, and A. L. Fetter, Vortex state in a d-wave superconductor, *Phys. Rev. B* **53**, 5795 (1996).
- [128] S. M. Young and B. J. Wieder, Filling-Enforced Magnetic Dirac Semimetals in Two Dimensions, *Phys. Rev. Lett.* **118**, 186401 (2017).
- [129] S. Guan, Y. Liu, Z.-M. Yu, S.-S. Wang, Y. Yao, and S. A. Yang, Two-dimensional spin-orbit Dirac point in monolayer HfGeTe , *Phys. Rev. Mater.* **1**, 054003 (2017).
- [130] S. Li, Y. Liu, S.-S. Wang, Z.-M. Yu, S. Guan, X.-L. Sheng, Y. Yao, and S. A. Yang, Nonsymmorphic-symmetry-protected hourglass Dirac loop, nodal line, and Dirac point in bulk and monolayer $X_3\text{SiTe}_6$ ($X = \text{Ta}, \text{Nb}$), *Phys. Rev. B* **97**, 045131

- (2018).
- [131] T. Sato, Z. Wang, K. Nakayama, S. Souma, D. Takane, Y. Nakata, H. Iwasawa, C. Cacho, T. Kim, T. Takahashi, and Y. Ando, Observation of band crossings protected by nonsymmorphic symmetry in the layered ternary telluride Ta_3SiTe_6 , *Phys. Rev. B* **98**, 121111 (2018).
- [132] Y. J. Jin, B. B. Zheng, X. L. Xiao, Z. J. Chen, Y. Xu, and H. Xu, Two-Dimensional Dirac Semimetals without Inversion Symmetry, *Phys. Rev. Lett.* **125**, 116402 (2020).
- [133] W. Meng, Y. Liu, W.-W. Yu, X. Zhang, and G. Liu, Spin-orbital robust Dirac points in two-dimensional systems, *Materials Today Physics* **27**, 100774 (2022).
- [134] L. Chen, L. Zhou, Y. Zhou, C. Liu, Z. Guo, K. Liao, S. Gao, W. Fan, J. Xu, Y. Guo, J. Wang, T. Qian, H. Weng, and G. Wang, Multiple Dirac points including potential spin-orbit Dirac points in nonsymmorphic $HfGe_{0.92}Te$, *Science China Physics, Mechanics & Astronomy* **66**, 217011 (2022).
-

Supplemental Material for “Intrinsic Second-Order Topological Superconductors with Tunable Majorana Zero Modes”

Xiao-Jiao Wang^{1,2,3}, Yijie Mo^{1,2,3}, Zhi Wang^{1,2}, Zhigang Wu^{4,*}, Zhongbo Yan^{1,2,3,†}

¹School of Physics, Sun Yat-sen University, Guangzhou 510275, China

²Guangdong Provincial Key Laboratory of Magnetoelectric Physics and Devices, Sun Yat-sen University, Guangzhou 510275, China

³State Key Laboratory of Optoelectronic Materials and Technologies, Sun Yat-sen University, Guangzhou 510275, China

⁴Quantum Science Center of Guangdong-Hong Kong-Macao Greater Bay Area (Guangdong), Shenzhen 508045, China

The supplemental material provides both bulk and boundary theories to understand the second-order topology and tunable Majorana zero modes (MZMs). Three sections are in order: (I) Topological configuration in momentum space and second-order topology; (II) Bulk topological invariant; (III) Edge-state theory for tunable MZMs.

I. TOPOLOGICAL CONFIGURATION IN MOMENTUM SPACE AND SECOND-ORDER TOPOLOGY

The principle of adiabatic continuity provides a powerful framework for analyzing the topological equivalence of gapped quantum phases. In essence, the principle asserts that two gapped phases are topologically equivalent if their respective Hamiltonians can be connected through a continuous path of parameters that never closes the energy gap and preserves the system’s symmetries. The utility of this approach stems from the fact that a topologically trivial limit is often known for a given Hamiltonian. Consequently, one can determine whether a gapped phase is topological by checking if it can be adiabatically connected to this trivial limit. If such a connection is possible, the phase is trivial; otherwise, it is topological.

For a Bogoliubov-de Gennes (BdG) Hamiltonian, the limit $\mu \rightarrow \pm\infty$ is always topologically trivial, as it corresponds to a state where all bands are either completely filled ($\mu = +\infty$) or completely empty ($\mu = -\infty$). Combining this fact with the principle of adiabatic continuity hence provides an efficient approach to determine whether a gapped superconducting state is topological or trivial. In the following, we apply this simple method to demonstrate that a superconducting state with two Dirac Fermi pockets gapped by opposite-sign pairing is necessarily topological.

We start from the normal-state Hamiltonian, which reads

$$\mathcal{H}(\mathbf{k}) = (\epsilon(\mathbf{k}) - \mu) + \eta(\mathbf{k})\sigma_x + 2\lambda_{\text{so}}\sigma_z(\sin k_x s_y - \sin k_y s_x). \quad (\text{S1})$$

The functions $\epsilon(\mathbf{k}) = -2t(\cos k_x + \cos k_y)$ and $\eta(\mathbf{k}) = 4[\eta_1 \cos(k_x/2)\cos(k_y/2) + \eta_2 \sin(k_x/2)\sin(k_y/2)]$ are defined for brevity. Here we have added the chemical potential μ to the Hamiltonian. Accordingly, the Fermi surface corresponds to the zero-energy contours of the energy spectrum. The explicit form of the energy spectrum is

$$E_{\pm}(\mathbf{k}) = (\epsilon(\mathbf{k}) - \mu) \pm \sqrt{\eta^2(\mathbf{k}) + 4\lambda_{\text{so}}^2(\sin^2 k_x + \sin^2 k_y)}. \quad (\text{S2})$$

Each band is doubly degenerate due to the conservation of \mathcal{PT} symmetry. In Fig. S1, we show the evolution of the Fermi surface with respect to μ , while keeping all other parameters fixed. At $\mu = 0$, the Fermi level crosses the two Dirac points located at $\mathbf{X} = (\pi, 0)$ and $\mathbf{Y} = (0, \pi)$, giving rise to two point-like Fermi surfaces. When μ is varied away from zero—either increased or decreased—two finite-sized Fermi pockets emerge, one enclosing \mathbf{X} and the other \mathbf{Y} . The two Fermi pockets will merge when $|\mu|$ is increased to a critical value, resulting in a Lifshitz transition of the Fermi surface. With a further increase of $|\mu|$, the Fermi surface will become a circle enclosing either Γ or \mathbf{M} . Since the band structure lacks Dirac points at these high-symmetry points, the Fermi surface shrinks continuously to a point and vanishes as $|\mu|$ is increased further.

Now we move to the superconducting state. Since the A_g pairing is favored, we focus on the BdG Hamiltonian corresponding to this pairing channel. Its general form is

$$\mathcal{H}_{\text{BdG}}(\mathbf{k}) = (\epsilon(\mathbf{k}) - \mu)\tau_z + \eta(\mathbf{k})\tau_z\sigma_x + 2\lambda_{\text{so}}(\sin k_x \tau_z \sigma_z s_y - \sin k_y \sigma_z s_x) + \Delta(\mathbf{k})\tau_y s_y. \quad (\text{S3})$$

The pairing term anticommutes with all other terms in the BdG Hamiltonian, and thus the BdG spectrum is simply given by

$$E_{\pm,\pm}(\mathbf{k}) = \pm \sqrt{\left[(\epsilon(\mathbf{k}) - \mu) \pm \sqrt{\eta^2(\mathbf{k}) + 4\lambda_{\text{so}}^2(\sin^2 k_x + \sin^2 k_y)} \right]^2 + \Delta^2(\mathbf{k})}. \quad (\text{S4})$$

It is readily seen that the energy gap closes only when the pairing node (momentums satisfying $\Delta(\mathbf{k}) = 0$) meets the Fermi surface. When the Fermi surface contains two Dirac Fermi pockets near \mathbf{X} and \mathbf{Y} , we have demonstrated that the pairing function

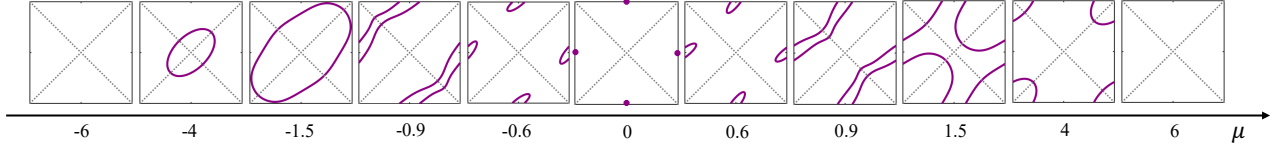


FIG. S1. Evolution of the Fermi surface (purple solid lines) in the first Brillouin zone with respect to the chemical potential μ . Starting from a configuration with two Dirac Fermi points ($\mu = 0$) separated by the pairing node lines (dashed lines), the Fermi surface cannot be made to vanish without crossing the pairing node lines. This indicates a topological configuration, as its adiabatic path to the trivial limit (without Fermi surface) is obstructed. Common parameters: $t = 0.5$, $\lambda_{\text{so}} = 0.4$, $\eta_1 = 0.8$, and $\eta_2 = 0.8$.

takes the $d_{x^2-y^2}$ -wave form [$\Delta(\mathbf{k}) = \Delta(\cos k_x - \cos k_y)$], resulting in a gapped superconducting state with opposite pairing signs on the two Fermi pockets. For this $d_{x^2-y^2}$ -wave function, the pairing nodes lie along the lines $k_x = k_y$ and $k_x = -k_y$, as indicated by the two dashed lines in Fig. S1. With the pairing nodes fixed, Fig. S1 clearly shows that the Fermi pockets enclosing the Dirac points cannot be adiabatically deformed to vanish without crossing the pairing node lines. This obstruction intuitively demonstrates that this gapped d -wave superconducting phase is topologically distinct from the trivial phase at $\mu = \pm\infty$ and must therefore be topological.

II. BULK TOPOLOGICAL INVARIANT

Having intuitively established the topological nature of the superconducting state with two Dirac Fermi pockets gapped by a d -wave pairing, we now quantify its character. By applying the principle of adiabatic continuity, below we demonstrate that this phase is a second-order topological superconductor, characterized by a quantized quadrupole moment.

We note that the BdG Hamiltonian commutes with the mirror symmetry operator $\tilde{\mathcal{M}}_z = i\tau_z\sigma_x s_z$, i.e., $[\mathcal{H}_{\text{BdG}}(\mathbf{k}), \tilde{\mathcal{M}}_z] = 0$. Therefore, it can be block-diagonalized into two sectors according to the $\pm i$ eigenvalues of $\tilde{\mathcal{M}}_z$: $\mathcal{H}_{\text{BdG}} = \mathcal{H}_{+i} \oplus \mathcal{H}_{-i}$. As these two mirror sectors are related by time-reversal symmetry, we can characterize the topology by focusing on a single sector. Without loss of generality, we choose \mathcal{H}_{+i} , whose explicit form is

$$\begin{aligned} \mathcal{H}_{+i}(\mathbf{k}) = & -(\Delta(\mathbf{k}) + \Delta_0)\tau_x\rho_z - 2\lambda_{\text{so}}(\sin k_x\rho_y - \sin k_y\rho_x) \\ & + (\epsilon(\mathbf{k}) - \mu)\tau_z + \eta(\mathbf{k})\tau_z\rho_z. \end{aligned} \quad (\text{S5})$$

To demonstrate the bulk-corner correspondence—the power of the bulk topological invariant to predict zero-energy corner states—we introduce an on-site s -wave component Δ_0 to the pairing function. This allows us to drive a direct transition between a second-order topological phase and a trivial phase simply by varying Δ_0 , while preserving all relevant symmetries.

In Fig. S1, the three middle configurations are topologically equivalent, as they can be adiabatically connected without closing the energy gap. This allows us to simplify the analysis by setting $\mu = 0$. Furthermore, at $\mu = 0$, the Fermi surfaces are point-like and unaffected by $\epsilon(\mathbf{k})$. We can therefore also set $t = 0$, thereby eliminating the $\epsilon(\mathbf{k})$ term from the Hamiltonian entirely.

When $t = 0$ and $\mu = 0$, the mirror Hamiltonian \mathcal{H}_{+i} reduces to

$$\mathcal{H}_{+i}(\mathbf{k}) = -(\Delta(\mathbf{k}) + \Delta_0)\tau_x\rho_z - 2\lambda_{\text{so}}(\sin k_x\rho_y - \sin k_y\rho_x) + \eta(\mathbf{k})\tau_z\rho_z. \quad (\text{S6})$$

We perform a unitary transformation to the Hamiltonian: $\mathcal{H}'_{+i} = W^\dagger \mathcal{H}_{+i} W$ with $W = e^{i\frac{\pi}{4}\tau_y}$, which yields

$$\mathcal{H}'_{+i}(\mathbf{k}) = (\Delta(\mathbf{k}) + \Delta_0)\tau_z\rho_z - 2\lambda_{\text{so}}(\sin k_x\rho_y - \sin k_y\rho_x) + \eta(\mathbf{k})\tau_x\rho_z. \quad (\text{S7})$$

This form of the Hamiltonian admits a straightforward real-space interpretation, enabling the definition of a real-space topological invariant. Since a topological invariant is a mathematical property of the Hamiltonian itself and is independent of how we interpret the Pauli matrices, we can freely assign them for computational convenience. We therefore assign the τ_i matrices to act on the sublattice degrees of freedom and the ρ_i matrices to act on an internal degree of freedom (such as spin).

It is readily seen that \mathcal{H}'_{+i} possesses chiral symmetry, with the symmetry operator given by $\mathcal{S} = \tau_y\rho_z$ and satisfying $\{\mathcal{H}'_{+i}, \mathcal{S}\} = 0$. This symmetry can quantize the quadrupole moment defined as [80, 81]:

$$q_{xy} = \left[\frac{1}{2\pi} \text{Im} \log[\det(U^\dagger \hat{Q} U)] - q_0 \right] \mod 1, \quad (\text{S8})$$

where $\hat{Q} = \text{diag} \left\{ e^{2\pi i \hat{x}_j \hat{y}_j / (L_x L_y)} \right\}_{j=1}^{4L_x L_y}$ with $\hat{x}_j (\hat{y}_j)$ denoting the x -position (y -position) operator for electron j , and the matrix U is constructed by column-wise packing all the occupied eigenstates of an $L_x \times L_y$ system under periodic boundary

conditions. Here, $q_0 = \frac{1}{4\pi} \text{Im} \log \det \hat{Q}$ is the contribution from the background positive charge distribution. When $q_{xy} = 1/2$, the gapped phase is a second-order topological phase characterized by the presence of zero-energy corner states when open boundary conditions are imposed along both x and y .

The quantization of q_{xy} can be proved as follows. First, one can rewrite Eq. (S8) as

$$\begin{aligned} q_{xy} &= \left[\frac{1}{2\pi} \text{Im} \log [\det(U^\dagger \hat{Q} U)] - q_0 \right] \bmod 1 \\ &= \left[\frac{1}{2\pi} \text{Im} \log [\det(U^\dagger \hat{Q} U)] - \frac{1}{4\pi} \text{Im} \log \det \hat{Q} \right] \bmod 1 \\ &= \left[\frac{1}{2\pi} \text{Im} \log [\det(U^\dagger \hat{Q} U)] + \frac{1}{2\pi} \text{Im} \log (\det \hat{Q}^\dagger)^{\frac{1}{2}} \right] \bmod 1 \\ &= \left[\frac{1}{2\pi} \text{Im} \log [\det(U^\dagger \hat{Q} U)] \sqrt{\det \hat{Q}^\dagger} \right] \bmod 1. \end{aligned} \quad (\text{S9})$$

Proving the quantization of the quadrupole moment is therefore equivalent to showing that chiral symmetry ensures the quantity $\det(U^\dagger \hat{Q} U) \sqrt{\det(\hat{Q}^\dagger)}$ is real [82]. To proceed, we deform the determinant as follows:

$$\begin{aligned} \det(U^\dagger \hat{Q} U) &= \det[U^\dagger(\hat{Q} - \mathbf{1} + \mathbf{1})U] \\ &= \det[\mathbf{1} + U^\dagger(\hat{Q} - \mathbf{1})U]. \end{aligned} \quad (\text{S10})$$

Applying Sylvester's determinant identity, $\det(\mathbf{1} + AB) = \det(\mathbf{1} + BA)$, simplifies the expression to

$$\det(U^\dagger \hat{Q} U) = \det(\mathbf{1} + (\hat{Q} - \mathbf{1})UU^\dagger). \quad (\text{S11})$$

Recognizing that $UU^\dagger = P_{\text{occ}}$ is the projection operator onto the occupied states, and that it can also be expressed as $P_{\text{occ}} = \mathbf{1} - VV^\dagger$ (where V is the matrix of unoccupied state eigenvectors), we derive the following relation:

$$\begin{aligned} \det(U^\dagger \hat{Q} U) &= \det[\mathbf{1} + (\hat{Q} - \mathbf{1})(\mathbf{1} - VV^\dagger)] \\ &= \det[\hat{Q} - (\hat{Q} - \mathbf{1})VV^\dagger] \\ &= \det[\mathbf{1} + (\hat{Q}^\dagger - \mathbf{1})VV^\dagger] \det \hat{Q} \\ &= \det(V^\dagger \hat{Q}^\dagger V) \det \hat{Q}. \end{aligned} \quad (\text{S12})$$

Now, we invoke chiral symmetry, defined by $\mathcal{SHS}^{-1} = -\mathcal{H}$. This symmetry implies a relation between the occupied and unoccupied eigenvector matrices:

$$V = \mathcal{S}U. \quad (\text{S13})$$

Using this relation, along with the commutation $[\mathcal{S}, \hat{Q}] = 0$ (note both matrices are diagonal), we can find

$$\begin{aligned} \det(U^\dagger \hat{Q} U) &= \det(V^\dagger \hat{Q}^\dagger V) \det \hat{Q} \\ &= \det(U^\dagger S^\dagger \hat{Q}^\dagger S U) \det \hat{Q} \\ &= \det(U^\dagger \hat{Q}^\dagger U) \det \hat{Q}. \end{aligned} \quad (\text{S14})$$

Since \hat{Q} is unitary, we have $\det(\hat{Q}) \det(\hat{Q}^\dagger) = \det(\hat{Q}\hat{Q}^\dagger) = 1$. Combining this with Eq. (S14) yields:

$$\det(U^\dagger \hat{Q} U) \sqrt{\det \hat{Q}^\dagger} = \det(U^\dagger \hat{Q}^\dagger U) \sqrt{\det \hat{Q}}. \quad (\text{S15})$$

Furthermore, using the property $\det(\hat{Q}) = [\det(\hat{Q}^\dagger)]^*$, we find:

$$\det(U^\dagger \hat{Q} U) \sqrt{\det \hat{Q}^\dagger} = \left(\det(U^\dagger \hat{Q} U) \sqrt{\det \hat{Q}^\dagger} \right)^*. \quad (\text{S16})$$

This equality confirms that $\det(U^\dagger \hat{Q} U) \sqrt{\det \hat{Q}^\dagger}$ is real. Consequently, the quadrupole moment q_{xy} is quantized to 0 or $1/2$, modulo 1.

Figure S2(a) shows the evolution of the quadrupole moment q_{xy} with respect to Δ_0 . The sharp change at $\Delta_0 \approx 0.55$ indicates a phase transition from a topological to a trivial gapped phase. To verify the bulk-corner correspondence, we compute the energy spectrum under open boundary conditions. For a representative topological phase with $q_{xy} = 1/2$, the spectrum in Fig. S2(b) reveals four zero-energy modes, with wavefunctions localized at the corners. This confirms a second-order topological phase. In contrast, for a trivial phase with $q_{xy} = 0$, Fig. S2(c) shows no in-gap states, confirming the bulk's trivial nature.

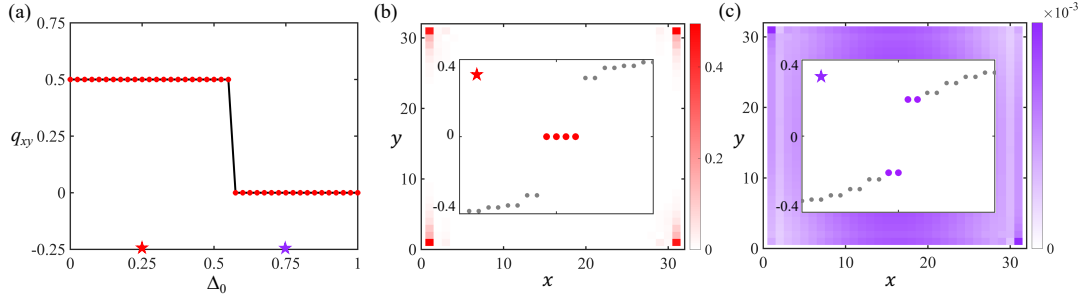


FIG. S2. (a) Evolution of the quadrupole moment q_{xy} with respect to Δ_0 . (b) Four zero-energy states are found in the spectrum when $\Delta_0 = 0.25$. Their wave functions are localized at the four corners of the full open-boundary system. (c) No zero-energy states are found when $\Delta_0 = 0.75$. Common parameters: $t = 0$, $\mu = 0$, $\lambda_{\text{so}} = 0.4$, $\eta_1 = 0.8$, $\eta_2 = 0.2$, and $\Delta = 0.3$.

III. EDGE-STATE THEORY FOR TUNABLE MZMS

Although the bulk topological invariant predicts the existence of MZMs at the corners under full open boundary conditions, it cannot explain the sensitive dependence of their positions on the sublattice termination. Here, ‘sublattice’ denotes the layer degree of freedom, which acts as a sublattice from a top-down view of the bilayer system. To explain this intriguing phenomenon, we develop an edge-state theory, which provides a natural framework for fully understanding the behavior of topological boundary states.

To derive the edge-state theory, we begin with the mirror-block Hamiltonians:

$$\begin{aligned} \mathcal{H}_{\pm i}(\mathbf{k}) = & (\epsilon(\mathbf{k}) - \mu)\tau_z + \eta(\mathbf{k})\tau_z\rho_z \mp \Delta(\mathbf{k})\tau_x\rho_z \\ & + 2\lambda_{\text{so}}(\mp \sin k_x\rho_y + \sin k_y\rho_x). \end{aligned} \quad (\text{S17})$$

Since the analysis for the two mirror sectors is identical, we focus on $\mathcal{H}_{+i}(\mathbf{k})$. We decompose this Hamiltonian into two parts: $\mathcal{H}_{+i}(\mathbf{k}) = \mathcal{H}_0(\mathbf{k}) + \mathcal{H}_p(\mathbf{k})$, where

$$\begin{aligned} \mathcal{H}_0(\mathbf{k}) = & -\Delta(\mathbf{k})\tau_x\rho_z - 2\lambda_{\text{so}}(\sin k_x\rho_y - \sin k_y\rho_x), \\ \mathcal{H}_p(\mathbf{k}) = & (\epsilon(\mathbf{k}) - \mu)\tau_z + \eta(\mathbf{k})\tau_z\rho_z. \end{aligned} \quad (\text{S18})$$

We will treat \mathcal{H}_p as a perturbation. Although the energy scale of \mathcal{H}_p in realistic materials may be larger than that of \mathcal{H}_0 , this approach is formally justified due to the principle of adiabatic continuity. Specifically, we can introduce a small, dimensionless parameter α to continuously tune the perturbation to $\alpha\mathcal{H}_p(\mathbf{k})$. This deformation preserves the system’s symmetries and, crucially, does not close the bulk energy gap, thereby leaving the topology invariant. Because the topological physics is qualitatively unchanged under the adiabatic connection to $\alpha\mathcal{H}_p$ for small α , we treat \mathcal{H}_p directly as a perturbation.

Since the system has a bipartite-lattice structure, there are two natural unit cell choices. Interestingly, they lead to distinct sublattice terminations at the same boundary, as shown in Figs. S3(a) and S3(b). Below, we demonstrate that this termination profoundly affects the boundary topology.

While directly solving for the edge-state wave functions of this lattice Hamiltonian is achievable, focusing on the low-energy regime simplifies the analysis of the boundary topology. To establish a low-energy theory, we again invoke the principle of adiabatic continuity. Specifically, we consider a deviation from the perfect d -wave pairing symmetry to the form $\Delta(\mathbf{k}) = \Delta \cos k_x - (\Delta + \delta) \cos k_y$, where both Δ and δ are positive constants and δ is assumed to be much smaller than all other energy scales. The introduction of this small parameter obviously affects neither the system’s underlying symmetries nor closes the bulk energy gap; therefore, it leaves the topology of the full Hamiltonian unchanged. However, this small deviation opens a finite gap in the spectrum of \mathcal{H}_0 , driving it into a weak topological insulator phase with helical edge states on the y -normal edges. Since \mathcal{H}_0 features two degenerate energy minima at $(0,0)$ and (π,π) , we perform a low-energy expansion around these two momenta, which yields:

$$\begin{aligned} \mathcal{H}_0(\mathbf{q})_{(0,0)} = & [\delta + \frac{\Delta}{2}q_x^2 - \frac{1}{2}(\Delta + \delta)q_y^2]\tau_x\rho_z - 2\lambda_{\text{so}}(q_x\rho_y - q_y\rho_x), \\ \mathcal{H}_0(\mathbf{q})_{(\pi,\pi)} = & -[\delta + \frac{\Delta}{2}q_x^2 - \frac{1}{2}(\Delta + \delta)q_y^2]\tau_x\rho_z + 2\lambda_{\text{so}}(q_x\rho_y - q_y\rho_x). \end{aligned} \quad (\text{S19})$$

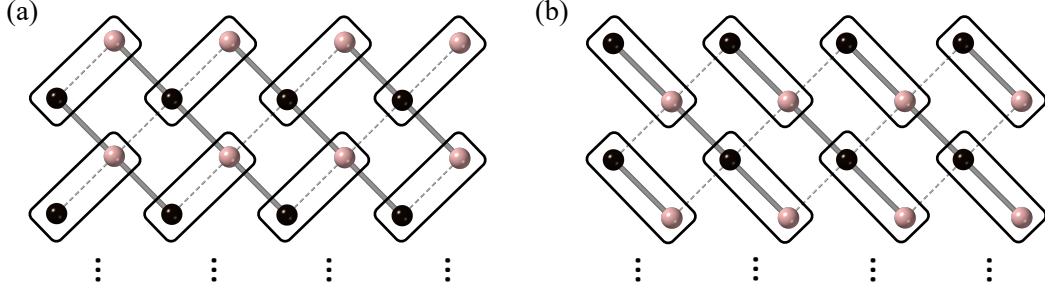


FIG. S3. Two distinct unit cell choices (rectangles) result in different sublattice terminations under open boundary conditions. (a) Type I: The unit cell leads to an upper edge with B-sublattice termination (pink dots). The sequence of sublattice is B-A-...-B-A from top to bottom. (b) Type II: The alternative unit cell gives A-sublattice termination (black dots) with sublattice sequence A-B-...-A-B. Bond conventions: solid lines for $\eta_+ = \eta_1 + \eta_2$, dashed lines for $\eta_- = \eta_1 - \eta_2$.

In the main text, we employ a Fourier transform convention that explicitly specifies the sublattice positions:

$$\begin{aligned} c_{\mathbf{R}_n, A} &= \sum_{\mathbf{k}} c_{\mathbf{k}, A} e^{i\mathbf{k} \cdot (\mathbf{R}_n + \delta_A)}, \\ c_{\mathbf{R}_n, B} &= \sum_{\mathbf{k}} c_{\mathbf{k}, B} e^{i\mathbf{k} \cdot (\mathbf{R}_n + \delta_B)}, \end{aligned} \quad (\text{S20})$$

where \mathbf{R}_n is the position of the n th unit cell, and $\delta_{A/B}$ are the basis vectors for the two sublattices. In this convention, the $\eta(\mathbf{k})$ term in the normal-state Hamiltonian takes the form

$$\mathcal{H}_\eta(\mathbf{k}) = \begin{pmatrix} 0 & 0 & \eta(\mathbf{k}) & 0 \\ 0 & 0 & 0 & \eta(\mathbf{k}) \\ \eta(\mathbf{k}) & 0 & 0 & 0 \\ 0 & \eta(\mathbf{k}) & 0 & 0 \end{pmatrix} = \eta(\mathbf{k}) \sigma_x s_0. \quad (\text{S21})$$

The function $\eta(\mathbf{k}) = 4(\eta_1 \cos(k_x/2) \cos(k_y/2) + \eta_2 \sin(k_x/2) \sin(k_y/2))$ has the property $\eta(\mathbf{k} + \mathbf{G}_x) = \eta(\mathbf{k} + \mathbf{G}_y) = -\eta(\mathbf{k})$, where $\mathbf{G}_x = (2\pi, 0)$ and $\mathbf{G}_y = (0, 2\pi)$ are reciprocal lattice vectors. Consequently, the full Hamiltonian is not periodic in the first Brillouin zone: $\mathcal{H}(\mathbf{k} + \mathbf{G}_{x/y}) \neq \mathcal{H}(\mathbf{k})$. While the energy spectrum is independent of the Fourier transform convention, a periodic Hamiltonian is essential for a consistent topological analysis. We therefore adopt a convention that ensures $\mathcal{H}(\mathbf{k} + \mathbf{G}_x) = \mathcal{H}(\mathbf{k} + \mathbf{G}_y) = \mathcal{H}(\mathbf{k})$. This is achieved by defining the Fourier transform without the sublattice phase factors:

$$\begin{aligned} c_{\mathbf{R}_n, A} &= \sum_{\mathbf{k}} c_{\mathbf{k}, A} e^{i\mathbf{k} \cdot \mathbf{R}_n}, \\ c_{\mathbf{R}_n, B} &= \sum_{\mathbf{k}} c_{\mathbf{k}, B} e^{i\mathbf{k} \cdot \mathbf{R}_n}. \end{aligned} \quad (\text{S22})$$

With this convention, while intra-sublattice hopping and spin-orbit coupling terms retain their original form, the $\eta(\mathbf{k})$ term becomes dependent on the unit cell geometry. In the basis $\psi_{\mathbf{k}} = (c_{\mathbf{k}, A\uparrow}, c_{\mathbf{k}, A\downarrow}, c_{\mathbf{k}, B\uparrow}, c_{\mathbf{k}, B\downarrow})^T$ and for the type-I unit cell shown in Fig. S3(a), this term is given by

$$\mathcal{H}_\eta^{(I)}(\mathbf{k}) = \begin{pmatrix} 0 & 0 & g(\mathbf{k}) & 0 \\ 0 & 0 & 0 & g(\mathbf{k}) \\ g^*(\mathbf{k}) & 0 & 0 & 0 \\ 0 & g^*(\mathbf{k}) & 0 & 0 \end{pmatrix} \quad (\text{S23})$$

where

$$g(\mathbf{k}) = \eta_- + \eta_+ e^{-ik_x} + \eta_+ e^{-ik_y} + \eta_- e^{-ik_x - ik_y} \quad (\text{S24})$$

$$= e^{-i\frac{(k_x+k_y)}{2}} (4\eta_1 \cos \frac{k_x}{2} \cos \frac{k_y}{2} + 4\eta_2 \sin \frac{k_x}{2} \sin \frac{k_y}{2})$$

$$= e^{-i\frac{(k_x+k_y)}{2}} \eta(\mathbf{k}). \quad (\text{S25})$$

It is evident that now the full Hamiltonian is periodic since $g(\mathbf{k} + \mathbf{G}_{x/y}) = g(\mathbf{k})$. Also in the basis $\psi_{\mathbf{k}} = (c_{\mathbf{k},A\uparrow}, c_{\mathbf{k},A\downarrow}, c_{\mathbf{k},B\uparrow}, c_{\mathbf{k},B\downarrow})^T$ and for the unit cell shown in Fig. S3(b), the form becomes

$$\mathcal{H}_{\eta}^{(II)}(\mathbf{k}) = \begin{pmatrix} 0 & 0 & f(\mathbf{k}) & 0 \\ 0 & 0 & 0 & f(\mathbf{k}) \\ f^*(\mathbf{k}) & 0 & 0 & 0 \\ 0 & f^*(\mathbf{k}) & 0 & 0 \end{pmatrix} \quad (\text{S26})$$

where

$$\begin{aligned} f(\mathbf{k}) &= \eta_+ + \eta_- e^{-ik_x} + \eta_- e^{ik_y} + \eta_+ e^{-ik_x+ik_y} \\ &= e^{-i\frac{(k_x-k_y)}{2}} (4\eta_1 \cos \frac{k_x}{2} \cos \frac{k_y}{2} + 4\eta_2 \sin \frac{k_x}{2} \sin \frac{k_y}{2}) \\ &= e^{-i\frac{(k_x-k_y)}{2}} \eta(\mathbf{k}). \end{aligned} \quad (\text{S27})$$

The two unit cell choices differ only by a phase factor. As shown below, this phase difference critically influences the boundary Dirac mass.

To construct a low-energy theory, we expand $\mathcal{H}_{\eta}^{(I,II)}(\mathbf{k})$ to leading order around the two low-energy points, $(0,0)$ and (π,π) , obtaining:

$$\begin{aligned} \mathcal{H}_{\eta}^{(I)}(\mathbf{q})_{(0,0)} &= 4\eta_1 \sigma_x s_0, \\ \mathcal{H}_{\eta}^{(I)}(\mathbf{q})_{(\pi,\pi)} &= -4\eta_2 \sigma_x s_0, \\ \mathcal{H}_{\eta}^{(II)}(\mathbf{q})_{(0,0)} &= 4\eta_1 \sigma_x s_0, \\ \mathcal{H}_{\eta}^{(II)}(\mathbf{q})_{(\pi,\pi)} &= 4\eta_2 \sigma_x s_0. \end{aligned} \quad (\text{S28})$$

Consequently, in the superconducting state, the perturbative Hamiltonians (to leading order) for the two unit cell choices are:

$$\begin{aligned} \mathcal{H}_p^{(I)}(\mathbf{q})_{(0,0)} &= (-4t - \mu)\tau_z + 4\eta_1 \tau_z \rho_z, \\ \mathcal{H}_p^{(I)}(\mathbf{q})_{(\pi,\pi)} &= (4t - \mu)\tau_z - 4\eta_2 \tau_z \rho_z, \\ \mathcal{H}_p^{(II)}(\mathbf{q})_{(0,0)} &= (-4t - \mu)\tau_z + 4\eta_1 \tau_z \rho_z, \\ \mathcal{H}_p^{(II)}(\mathbf{q})_{(\pi,\pi)} &= (4t - \mu)\tau_z + 4\eta_2 \tau_z \rho_z. \end{aligned} \quad (\text{S29})$$

Since \mathcal{H}_0 consists entirely of intra-sublattice terms, it is identical for the two unit cell choices.

Next, we derive the low-energy edge-state Hamiltonian corresponding to each low-energy bulk Hamiltonian. We begin with

$$\begin{aligned} \mathcal{H}_0^{(I)}(\mathbf{q})_{(0,0)} &= [\delta + \frac{\Delta}{2} q_x^2 - \frac{1}{2}(\Delta + \delta)q_y^2]\tau_x \rho_z - 2\lambda_{\text{so}}(q_x \rho_y - q_y \rho_x), \\ \mathcal{H}_p^{(I)}(\mathbf{q})_{(0,0)} &= (-4t - \mu)\tau_z + 4\eta_1 \tau_z \rho_z. \end{aligned} \quad (\text{S30})$$

We now derive the edge states for the upper y -normal edge. For simplicity, consider the system in the half-infinite plane with $y \leq 0$, such that the upper edge corresponds to $y = 0$. Solving the eigenvalue equation $\mathcal{H}_0^{(I)}(q_x, q_y \rightarrow -i\partial_y)_{(0,0)}\psi_{\alpha}(x, y) = E_{\alpha}\psi_{\alpha}(x, y)$ under the boundary conditions $\psi_{\alpha}(x, 0) = \psi_{\alpha}(x, -\infty) = 0$ yields two branches of edge states. The first has a linear dispersion $E_1 = vq_x$ with velocity $v = 2\lambda_{\text{so}}$, and a wave function given by [87]

$$\psi_1(x, y) = \mathcal{N} \sin(\kappa_1 y) e^{iq_x x} |\chi_1\rangle. \quad (\text{S31})$$

Here, $|\chi_1\rangle = |\tau_x = 1, \rho_y = -1\rangle$ is an eigenvector of $\tau_x \rho_y$, and $\mathcal{N} = 2\sqrt{|\kappa_2(\kappa_1^2 + \kappa_2^2)/\kappa_1^2|}$ is the normalization constant, with $\kappa_1 = \sqrt{(2\delta + \Delta q_x^2)/(\Delta + \delta) - v^2/(\Delta + \delta)^2}$ and $\kappa_2 = v/(\Delta + \delta)$ (we have taken all coefficients to be positive for discussion convenience). The second branch has the opposite chirality, with dispersion $E_2 = -vq_x$ and wave function

$$\psi_2(x, y) = \mathcal{N} \sin(\kappa_1 y) e^{iq_x x} |\chi_2\rangle, \quad (\text{S32})$$

where $|\chi_2\rangle = |\tau_x = -1, \rho_y = 1\rangle$. Thus, before including perturbations, the low-energy edge-state Hamiltonian in the basis $(\psi_1, \psi_2)^T$ is

$$\mathcal{H}^{(I)}(q_x)_{(0)} = vq_x \zeta_z, \quad (\text{S33})$$

where ζ_i are Pauli matrices in the two-dimensional Hilbert space spanned by the edge states. Projecting the perturbation Hamiltonian $\mathcal{H}_p^{(I)}$ onto this subspace gives

$$\int_{-\infty}^0 \psi_\alpha^\dagger(x, y) \mathcal{H}_p^{(I)}(q_x, -i\partial_y)_{(0,0)} \psi_\beta(x, y) dy = (4\eta_1 \zeta_x)_{\alpha\beta}. \quad (\text{S34})$$

Consequently, the full low-energy edge-state Hamiltonian for this case is

$$\mathcal{H}^{(I)}(q_x)_{(0)} = vq_x \zeta_z + m_1 \zeta_x, \quad (\text{S35})$$

with Dirac mass $m_1 = 4\eta_1$. Notably, the $(-4t - \mu)\tau_z$ term does not contribute to the boundary Hamiltonian, indicating its irrelevance to the topological boundary physics in this regime. This finding provides an intuitive justification for neglecting this term when calculating the bulk topological invariant in Sec. II.

The same procedure applies to the other three cases, yielding the low-energy edge-state Hamiltonians:

$$\begin{aligned} \mathcal{H}^{(I)}(q_x)_{(\pi)} &= -vq_x \zeta_z - m_2 \zeta_x, \\ \mathcal{H}^{(II)}(q_x)_{(0)} &= vq_x \zeta_z + m_1 \zeta_x, \\ \mathcal{H}^{(II)}(q_x)_{(\pi)} &= -vq_x \zeta_z + m_2 \zeta_x, \end{aligned} \quad (\text{S36})$$

with Dirac mass $m_2 = 4\eta_2$ and the same basis $(\psi_1, \psi_2)^T$.

Each low-energy edge-state Hamiltonian possesses chiral symmetry ($\mathcal{S} = \zeta_y$), allowing characterization by a winding number:

$$W_\beta^{(a)} = \frac{i}{4\pi} \int_{-\infty}^{\infty} dq_x \text{Tr}\{\mathcal{S}[\mathcal{H}^{(a)}(q_x)_{(\beta)}]^{-1} \partial_{q_x} \mathcal{H}^{(a)}(q_x)_{(\beta)}\}, \quad (\text{S37})$$

where $a \in \{I, II\}$ and $\beta \in \{0, \pi\}$. Assuming $\eta_1, \eta_2 > 0$, a direct calculation gives:

$$\begin{aligned} W_0^{(I)} &= \frac{1}{2}, W_\pi^{(I)} = \frac{1}{2}; \\ W_0^{(II)} &= \frac{1}{2}, W_\pi^{(II)} = -\frac{1}{2}. \end{aligned} \quad (\text{S38})$$

The winding number characterizing the full edge is $W_T^{(a)} = W_0^{(a)} + W_\pi^{(a)}$. For the type-I edge in Fig. S3(a), we find:

$$W_T^{(I)} = W_0^{(I)} + W_\pi^{(I)} = 1, \quad (\text{S39})$$

while for the type-II edge shown in Fig. S3(b):

$$W_T^{(II)} = W_0^{(II)} + W_\pi^{(II)} = 0. \quad (\text{S40})$$

Since the only difference between the edges in Figs. S3(a) and S3(b) is their outermost sublattice, the different values for $W_T^{(I)}$ and $W_T^{(II)}$ indicate that the boundary topology depends sensitively on the sublattice termination. Consequently, when an edge contains segments with different sublattice terminations (A versus B), their interface forms a *sublattice domain wall* [118–120]. Across this topological defect, the winding number changes by $\Delta W_T = |W_T^{(I)} - W_T^{(II)}| = 1$. According to bulk-defect correspondence [117], this winding number difference dictates the number of zero-energy bound states at the defect. With $\Delta W_T = 1$ per mirror sector, each sublattice domain wall binds two zero-energy states. This winding-number analysis based on low-energy theory explains why MZM positions in this system can be manipulated by engineering the sublattice termination.

